Chemical Heterogeneity in a Single Phase: $Bi_{0.15}Ca_{0.85}MnO_3$, a Case Example of Macroscopic Phase Segregation

A. Llobet, C. Frontera, and J. L. García-Muñoz

Institut de Ciencia de Materials de Barcelona, CSIC, Campus de la UAB, 08193 Bellaterra, Spain

C. Ritter

Institut Laue-Langevin, 38042 Grenoble-Cedex, France

M. A. G. Aranda*

Departamento de Química Inorgánica, Universidad de Málaga, 29071 Málaga, Spain

Received June 1, 2000

Ultrahigh-resolution synchrotron diffraction for "$Bi_{0.15}Ca_{0.85}MnO_3$" at 300 K shows a unique pattern broadened by microstrains. The joint Rietveld refinement of synchrotron and neutron data at RT (room temperature) indicates that this phase is nonstoichiometric due to calcium vacancies. However, the synchrotron pattern at 10 K shows two phases one being monoclinic and the other orthorhombic. The refined weight fractions were 67.7(6) and 28.8(3)%, respectively. The joint Rietveld refinement at low temperature has established that this macroscopic phase separation/segregation is due to different thermal evolutions of the heterogeneous material. Orthorhombic and monoclinic low-temperature phases have different calcium contents. The sample at RT is formed by small domains (∼2000 Å) with minor variations in the cation stoichiometry, but it displays a single orthorhombic $GdFeO_3$-type powder pattern. The structural transition driven by the orbital ordering unmasks these domains, and the macroscopic phase segregation comes suddenly into sight. The associated structural changes and magnetic structures are reported. A unique pattern above the orbital ordering temperature (RT in most cases) is not any longer a proof of chemical homogeneity, or single phase existence, in manganites. So, the discussion of many previously reported data for manganites should be revisited.

Introduction

Mixed-valence perovskites and related oxides have exotic properties such as high-T_C superconductivity, colossal magnetoresistance CMR,[1] and metal−insulator transitions which are associated with orbital (and charge) ordering/disordering phenomena. The discovery of CMR in $A_{1-x}M_xMnO_3$ manganites (A = trivalent cation, M = divalent cation) has led to an explosion of interest in the tendency displayed by many manganites, and others transition metal oxides, to form inhomogeneous/segregated states. In this context, it is important to distinguish between nanoscopic phase segregation (electronic phase separation, stripes, and charge-ordering (CO) phenomena in general),[2−4] where the length scales are of the order of 3−20 Å, from macroscopic phase separation where the length scales are larger than 1000 Å.[5−7] CO is formed due to a strong repulsion between charge carriers. Oppositely, the formation of two nanoscopic regions of rich and poor density of charge carriers is related to a strong attractive interactions. Its origin can be, for instance, strain effects that try to minimize the lattice energy. The existence of orbital degeneration associated with the charges, and the strong electron−phonon coupling due to the Jahn−Teller distortions of the Mn^{3+} octahedra, are of capital importance to explain phase segregation. The strong relationship between CMR and phase separation makes nanoscopic and macroscopic phase segregation a current hot topic that deserves much attention. In manganese oxides, electronic phase separation has been theoretically proposed to occur in both the lightly ($0.1 < x < 0.2$) and heavily (0.75−0.95) doped regions of the phase diagram. In this work we explore the origins of macroscopic phase segregation.

* To whom correspondence should be addressed. E-mail: g_aranda@uma.es.

(1) Jin, S.; Tiefel, T. H.; McCormack, M.; Fastnacht, R. A.; Schultz, L.; Samwer, K. *Science* **1994**, *264*, 413.
(2) Radaelli, P. G.; Cox, D. E.; Marezio, M.; Cheong, S.-W. *Phys. Rev. B* **1997**, *55*, 3015.
(3) Moreo, A.; Yunoki, S.; Dagotto, E. *Science* **1999**, *283*, 2034.
(4) Mori, S.; Chen, C. H.; Cheong, S.-W. *Nature* **1998**, *392*, 473. Goodenough, J. B.; Zhou, J.-S. *Nature* **1997**, *386*, 229.
(5) Littlewood, P. *Nature* **1999**, *399*, 529.
(6) Uehara, M.; Mori, S.; Chen, C. H.; Cheong, S.-W. *Nature* **1999**, *399*, 560.
(7) Fäth, M.; Freisem, S.; Menovsky, A. A.; Tomioka, Y.; Aarts, J.; Mydosh, J. A. *Science* **1999**, *285*, 1540.

10.1021/cm000440p CCC: $19.00
Published on Web 11/16/2000

There are many reports of phase coexistence at low temperature in materials that display a single diffraction pattern at high temperature. High and low temperatures are those above and below a certain phase transition temperature, respectively. These transitions are usually due to orbital (and sometimes charge) ordering [T_{OO} and T_{CO}] and range between 100 and 475 K. So, in this context, high temperature is usually room temperature. Some examples of reports showing this dual behavior are the following: $Pr_{0.6}Sr_{0.4}MnO_3$;[8] $Pr_{0.5}Sr_{0.5}MnO_3$;[9] $Nd_{0.25}La_{0.25}Ca_{0.5}MnO_3$;[10] $La_{0.53}Ca_{0.47}MnO_3$;[11] $Sm_{0.15}Ca_{0.85}MnO_3$;[12] $Nd_{0.5}Sr_{0.5}MnO_3$.[13] This latter example deserves further attention as two samples with the same nominal stoichiometry were cautiously prepared and studied using high-resolution synchrotron powder diffraction. Both samples displayed a single phase at room temperature, but one showed a single pattern and the other three phases at low temperature.[13] This unusual behavior was interpreted in terms of compositional fluctuations in one sample although the joint X-ray and neutron refinements did not show a conclusive answer.

Low-temperature phase coexistence/separation has important implications in CMR and other properties. For example, there are several reports of a single low-temperature nuclear phase showing two sets of magnetic diffraction peaks.[12,14] With high-resolution diffraction data two nuclear phases can be distinguished, making possible the assignment of each magnetic structures to its nuclear cell. However, without such data, an alternative justification of all magnetic peaks, arising from a unique nuclear phase with a canted magnetic structure, is possible but can be wrong.

The purpose of this work has been to study the origin of macroscopic phase segregation in manganese perovskites by using ultrahigh-resolution synchrotron X-ray powder diffraction, SXRPD, data. The BM16 diffractometer[15] (at ESRF) has extremely high resolution, and it allows one to characterize this macroscopic phase segregation properly. Joint high energy-SXRPD and neutron powder diffraction, NPD, Rietveld refinements are essentially free from systematic errors if crystal analyzers are used in the scattered X-ray beam. Both diffraction experiments are carried out in transmission with the full sample tested by the probing radiation. X-rays extinction and absorption is not a problem if the energy of the experiment is high enough, usually above 25 keV for samples with heavy elements. In some special cases, due to the contrast given by X-ray and neutron, joint refinements can yield even better results than single-crystal laboratory X-ray diffraction data.[16] The resolution of the NPD data is poor when compared with that in the SXRPD pattern, and although the scattering power does not decrease with the scattering angle, the high incident intensity of the synchrotron radiation allows one to collect useful data up to lower *d* spacings. However, NPD data are outstanding because the scattering power of the sample/phase is evenly shared between all atoms. This is not the case in (S)XRPD where heavy elements dominate the scattering of the sample. So, NPD is essential to scale the refinements when stoichiometry may vary and, obviously, to locate precisely the positions of light elements. The joint refinement,[17] when properly carried out, uses all information embedded in the diffraction data, and it allows one to obtain the best structural description including subtle compositional details.

On the other hand, bismuth-containing manganites, $Bi_{1-x}A_xMnO_3$, are of interest since the lone pair of Bi^{3+} may play an important role in the electric and magnetic properties. The $Bi_{1-x}Ca_xMnO_3$ highly doped series has very recently been reported displaying a rich electrical and magnetic behavior.[18] Moreover, $Bi_{1/2}Sr_{1/2}MnO_3$ displays charge ordering at an extraordinarily high temperature of 475 K which has been justified due to the effects of the Bi^{3+} lone pair.[19]

In this work, we report first the room-temperature structural characterization of "$Bi_{0.15}Ca_{0.85}MnO_3$", which is shown to be slightly calcium deficient displaying a single orthorhombic diffraction pattern even with ultrahigh-resolution SXRPD data. However, two phases are detected at low temperature and the joint SXRPD and NPD Rietveld refinement indicates that this behavior is due to chemical heterogeneity in the sample. So, this study imposes a large strain on the routine association of a single pattern being due to a homogeneous phase in manganites. These results represent a step forward for a detailed understanding of macroscopic phase segregation in these fascinating materials.

Experimental Section

Synthesis. Polycrystalline $Bi_{0.15}Ca_{0.85}MnO_3$ was prepared by standard solid-state ceramic synthesis in air with several mechano-thermal cycles to ensure sample homogeneity. The starting compounds were Bi_2O_3, $CaCO_3$, and MnO_2. The stoichiometric mixture was thoroughly grounded in an agate mortar, pelletized, and initially heated at 1000 °C for 15 h. This treatment (grinding, pelletization, and heating) was repeated. Then, a third similar treatment was carried out at higher temperature, 1250 °C. Finally, a fourth cycle, also at 1250 °C but for 24 h, was applied. All heating and cooling rates were 300 °C/h. The resulting black polycrystalline sample had the typical $GdFeO_3$ pervoskite type X-ray laboratory powder diffraction pattern.

Techniques. *Ultrahigh-resolution synchrotron powder X-ray diffraction* (SXRPD) patterns were collected on BM16

(8) Ritter, C.; Radaelli, P. G.; Lees, M. R.; Barrat, J.; Balakrishnan, G.; Paul, M. D. K. *J. Solid State Chem.* **1996**, *127*, 276.
(9) Damay, F.; Martin, C.; Hervieu, M.; Maignan, A.; Raveau, B.; Andre, G.; Bouree, F. *J. Magn. Magn. Mater.* **1998**, *184*, 71.
(10) Arulraj, A.; Biswas, A.; Raychaudhuri, A. K.; Rao, C. N. R.; Woodward, P. M.; Vogt, T.; Cox, D. E.; Cheetham, A. K. *Phys. Rev. B* **1998**, *57*, R8115.
(11) Rhyne, J. J.; Kaiser, H.; Luo, H.; Xiao, G.; Gardel, M. L. *J. Appl. Phys.* **1998**, *83*, 7339.
(12) Martin, C.; Maignan, A.; Hervieu, M.; Raveau, B.; Jirák, Z.; Kurbakov, A.; Trounov, V.; Andre, G.; Bouree, F. *J. Magn. Magn. Mater.* **1999**, *205*, 184.
(13) Woodward, P. M.; Cox, D. E.; Vogt, T.; Rao, C. N. R.; Cheetham, A. K. *Chem. Mater.* **1999**, *11*, 3529.
(14) See for example: (a) Hervieu, M.; Martin, C.; Maignan, A.; Van Tendeloo, G.; Jirak, Z.; Hejtmanek, J.; Barnabe, A.; Thopart, D.; Raveau, B. *Chem. Mater.* 2000, *12*, 1456. (b) Frontera, C.; Garcia-Muñoz, J. L.; Llobet, A.; Respaud, M.; Broto, J. M.; Lord, J. S.; Planes, A. *Phys. Rev. B* **2000**, *62*, 3381.
(15) Fitch, A. N. *Mater. Sci. Forum* **1996**, *228−231*, 219. Hodeau, J. L.; Bordet, P.; Anne, M.; Prat, A.; Fitch, A. N.; Dooryhee, E.; Vaughan, G.; Freund, A. *SPIE Proc.* **1998**, *3448*, 353.
(16) Aranda, M. A. G.; Attfield, J. P. *Angew. Chem., Int. Ed. Engl.* **1993**, *32*, 1454.
(17) Williams, A.; Von Dreele, R. B.; Bish, D. L.; Kwei, G. H.; Larson, A. C.; Raistrick, I. D. *Phys. Rev. B* **1988**, *37*, 7960.
(18) Santhosh, P. N.; Goldberger, J.; Woodward, P. M.; Vogt, T.; Lee, W.; Epstein, A. *Phys. Rev. B* **2000**, in press.
(19) Garcia-Muñoz, J. L.; Frontera, C.; Aranda, M. A. G.; Llobet, A.; Ritter, C. *Phys. Rev. Lett.* **2000**, submitted for publication.

powder diffractometer of ESRF (Grenoble, France) in Debye−Scherrer (transmission) configuration at $T = 300$ and 10 K. $Bi_{0.15}Ca_{0.85}MnO_3$ was loaded in a borosilicate glass capillary ($\phi = 0.5$ mm) and rotated during data collection. A short wavelength, 0.442 377(2) Å (≡28.03 keV), was selected with a double-crystal Si (111) monochromator and calibrated with Si NIST. The standard cryostat was used, and the size of the beam on sample, measured with a film, was ∼7 mm wide and ∼0.7 mm height. The detectors system contains nine Ge(111) crystal analyzers between the sample and the nine point detectors. Each run between 4 and 38° (2θ) lasted $3^1/_2$ h, and the data from the detectors were normalized and summed up to 0.004° step size with local software to produce the raw data.

Neutron powder diffraction (NPD) patterns were collected on D2B powder diffractometer of ILL (Grenoble, France) at 4 and 300 K. D2B was used in the "high-intensity" mode with $\lambda = 1.594$ Å. The standard orange cryostat was used for temperature control. Temperature-dependent data were collected on the high-intensity D20 diffractometer operating with $\lambda = 2.42$ Å. A long wavelength permits a good resolution in the low 2θ angular range. This allowed us to follow the evolution of the magnetic structures and of the cell parameters.

Results

HT Rietveld Study. The crystal structure of $Bi_{0.15}Ca_{0.85}MnO_3$ at 300 K was refined by the Rietveld method using as starting model the orthorhombic $GdFeO_3$ type structure, space group *Pnma*, adequately modified to account for the sample stoichiometry. A joint refinement of the synchrotron and neutron data sets was carried out using the GSAS suite of programs.[20] First, the common overall parameters, scale factors, background coefficients, unit cell parameters, zero-shift errors and pseudo-Voigt coefficients,[21] corrected for asymmetry[22] were optimized. A minor side phase, $CaMn_2O_4$, was detected and accounted for appropriately. Its refined weight ratio was 3.6(1)%. To correct for minor differences in the collecting temperatures of both patterns, the neutron wavelength was refined.

The fwhm of the SXRPD peaks of the high-temperature orthorhombic phase, $Bi_{0.15}$-O-HT, was invariably dominated by sample-dependent effects. In similar experimental conditions, the peak width due to the instrumental contribution is calculated to be ∼0.003° neglecting the broadening due to the axial divergency. The lowest measured fwhm value has been 0.004° for $Na_2Ca_3Al_2F_{14}$.[23] For $Bi_{0.15}$-O-HT, nonoverlapping peaks such as (111) at 7.55° and (113) at 12.20° have fwhm values of 0.023 and 0.024°, respectively. The Gaussian contribution to the peak shape was very small, GW ∼ 0.1 [$(0.01°)^2$ units], and the Lorentzian contribution due to microstrains was very high with LY ∼ 15 (0.01° units) with negligible Lorentzian Scherrer broadening, LX < 0.2 (0.01° units). The SXRPD pattern has anisotropically broadened peaks. This could be partially remedied by the ellipsoidal broadening correction implemented in GSAS, and other Rietveld programs, by refining the STEC parameter with the [010] anisotropic direction. Once defined for the main ellipse direction, this parameter (STEC) distributes the fwhm of different (*hkl*) reflections appropriately. However, when the anisotropic microstrain broadening is dominant, the methodology developed by Rodriguez-Carvajal[24] and later generalized by Stephens[25] yields much better fits. This formalism has been recently incorporated in the GSAS code as function no. 4.

Table 1. Unit Cell and Peak Shape Parameters for the Perovskites Phases[a]

	phase O-HT	phase O-LT	phase M-LT[b]
a/Å	5.32805(2)	5.32020(5)	5.341 99(4)
b/Å	7.50419(3)	7.48221(6)	7.443 68(4)
c/Å	5.30199(2)	5.28373(4)	5.308 76(3)
V/Å^3	211.988(2)	210.329(3)	211.060(3)
eta	0.856(3)	0.715(9)	1.00
S_{200}	0.560(5)	0.59(2)	0.511(7)
S_{020}	0.095(9)	0.086(3)	0.038(1)
S_{002}	0.460(6)	0.178(8)	0.408(8)
S_{220}	0.128(3)	0.079(8)	0.123(4)
S_{202}	0.531(7)	0.25(1)	1.05(1)
S_{022}	0.130(5)	0.155(7)	0.152(4)
S_{301}			−0.52(2)
S_{103}			−0.72(2)
S_{121}			0.080(6)

[a] GW = 0.1, S/L = 0.004, and H/L = 0.008, for all phases. [b] $\beta = 91.079(1)°$.

Table 2. Refined Structural Parameters for $Bi_{0.15}$-O-HT

atom	occ fac	x	y	z	U_{iso}
Bi	0.162(2)	0.03459(5)	1/4	0.0055(1)	0.007(1)
Ca	0.753(10)	0.03459	1/4	0.0055	0.007
Mn	1.0	0	0	1/2	0.0020(1)
O(1)	1.0	0.4875(2)	1/4	0.0676(3)	0.0060(3)
O(2)	1.0	0.2876(2)	0.3406(1)	0.7125(2)	0.0066(2)

Table 3. Selected Bond Distances (Å) and Angles (deg) for $Bi_{0.15}$-O-HT

A−O(1)	2.444(1)	A−O(2) × 2	2.603(1)	Mn−O(1) × 2	1.9111(3)
A−O(1)	2.335(2)	A−O(2) × 2	2.584(1)	Mn−O(2) × 2	1.919(1)
A−O(1)	2.941(1)	A−O(2) × 2	2.358(1)	Mn−O(2) × 2	1.915(1)
		Mn−O(1)−Mn	158.01(9)	Mn−O(2)−Mn	157.09(5)

Refining the atomic coefficients and positional and isotropic thermal parameters with the nominal composition did not yield a completely satisfactory refinement because some peaks had not the adequate intensity. As we carried out a joint refinement with X-ray and neutron data, we were able to refine the occupation factors of Bi and Ca without constraints, ca. freely. This clearly improved the fit of both patterns, and moreover, these peaks got the right intensity. The optimization of the Mn occupation factor did not improve the fit significantly, and the resulting value was close to 99%. Hence, this parameter was set to 1.0 and not refined.

The final joint refinement was excellent and it converged to $R_{WP} = 3.52$ and $R_F = 2.25\%$ for the SXRPD data and to $R_{WP} = 5.04$ and $R_F = 1.80\%$ for the NPD data. In Figure 1 are shown the fits of the SXRPD (a) and NPD (b) patterns. The unit cell parameters and the refined peak shape coefficients are given in Table 1, the refined atomic parameters in Table 2, and selected bond distances and angles in Table 3. As an example of the improvement of the fits when refining the cation stoichiometry, a selected region of the SXRPD Rietveld plot is displayed in Figure 2 showing the calculated intensities for both type of refinements.

(20) Larson, A. C.; Von Dreele, R. B. *Los Alamos Natl. Lab. Rep.* 1994, *LA-UR-86-748*.
(21) Thompson, P.; Cox, D. E.; Hasting, J. B. *J. Appl. Crystallogr.* **1987**, *20*, 79.
(22) Finger, L. W.; Cox, D. E.; Jephcoat, A. P. *J. Appl. Crystallogr.* **1994**, *27*, 892. Aranda, M. A. G.; Losilla, E. R.; Cabeza, A.; Bruque, S. *J. Appl. Crystallogr.* **1998**, *31*, 16.
(23) Masson, O. Presented at EPDIC VII, Barcelona, 2000. To be published in *Mater. Sci. Forum*.
(24) Rodriguez-Carvajal, J.; Fernandez-Diaz, M. T.; Martinez, J. L. *J. Phys. Condens. Mater.* **1991**, *3*, 3215.
(25) Stephens, P. W. *J. Appl. Crystallogr.* **1999**, *32*, 281.

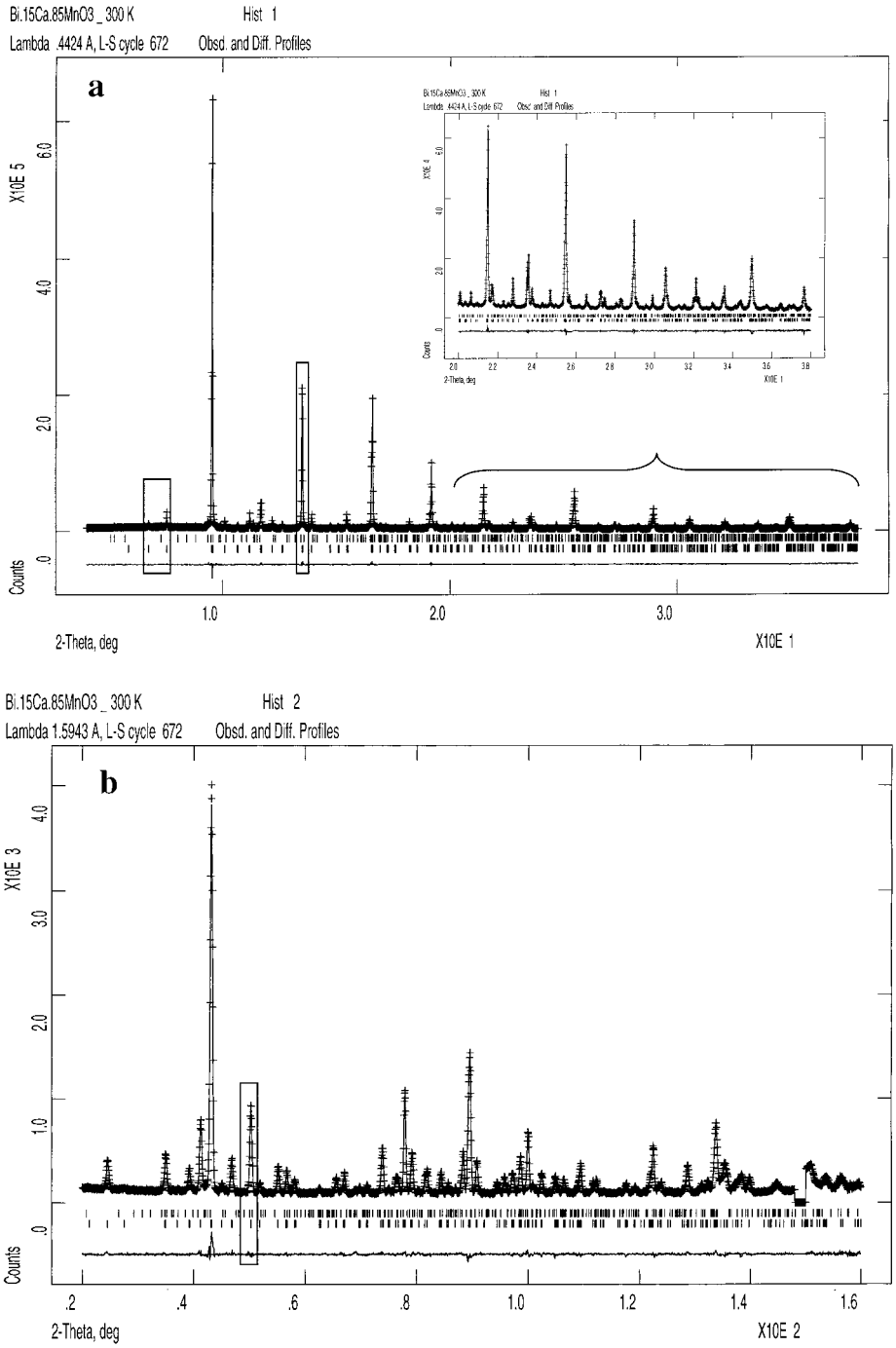

Figure 1. Observed (crosses), calculated, and difference SXRPD (a) and NPD (b) patterns for "$Bi_{0.15}Ca_{0.85}MnO_3$" at 300 K. Upper ticks are the allowed diffraction peaks for $CaMn_2O_4$ impurity phase, and the lower ticks are those of the $Bi_{0.15}$-O-HT phase. The inset shows the fit of the high-angle region (20−38°/2θ).

LT Rietveld Study. The SXRPD pattern of $Bi_{0.15}$-$Ca_{0.85}MnO_3$ at 10 K is very complex. A detailed inspection indicated the presence of the initial orthorhombic phase plus many other peaks. After subtraction of the peaks that were present in the RT (room temperature) pattern ($Bi_{0.15}$-O and $CaMn_2O_4$ phases), the remaining ones could be easily autoindexed using the TREOR90 program.[26] The cell parameters were $a = 5.311$ Å, $b = 7.450$ Å, $c = 5.341$ Å, and $\beta = 91.08°$ with figures of merit $M_{14} = 70$ and $F_{14} = 86$.[27] The modification of the *Pnma* symmetry to give the $P2_1/m$ one at LT (low temperature) with a small deviation of β angle from 90° has been previously reported in other manganites with similar doping levels.[12,28] The SXRPD and NPD patterns were analyzed by a joint refinement using GSAS. The NPD pattern was used between 48 and 160°/2θ to avoid the region where magnetic diffraction is important. Hence, a nuclear three-phase refinement (including $CaMn_2O_4$) was carried out using the strategy stated above. The coexistence of the pristine orthorhombic phase and the new monoclinic one is displayed in Figure

(26) Werner, P. E.; Eriksson, L.; Westdahl, M. *J. Appl. Crystallogr.* **1985**, *18*, 367.

(27) Wolff, P. M. *J. Appl. Crystallogr.* **1968**, *1*, 108. Smith, G. S.; Snyder, R. L. *J. Appl. Crystallogr.* **1979**, *12*, 60.

(28) Millange, F.; Caignaert, V.; Mather, G.; Suard, E.; Raveau, B. *J. Solid State Chem.* **1996**, *127*, 131.

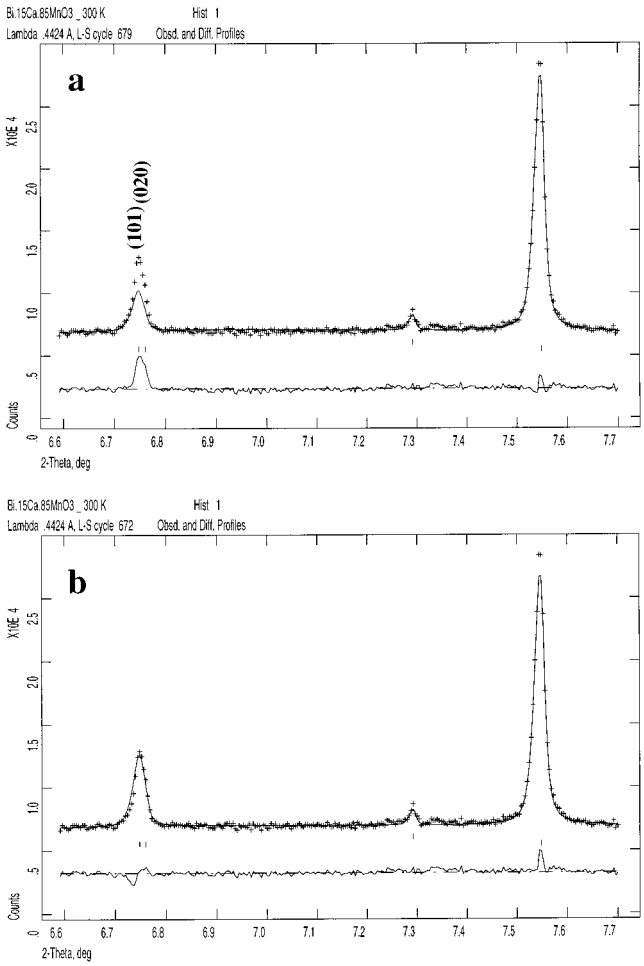

Figure 2. Selected region (6.6−7.7°/2θ) of the SXRPD Rietveld plot for "$Bi_{0.15}Ca_{0.85}MnO_3$" at 300 K with (a) nominal stoichiometry and (b) refining freely the occupation factors of the cations at the A site of the perovskite.

3 for SXRPD data. The same *d* spacing region is shown in Figure 4 for NPD data.

The peak shape of the low-temperature monoclinic phase, $Bi_{0.15}$-M-LT, is much more anisotropic than that of the low-temperature orthorhombic phase, $Bi_{0.15}$-O-LT. This is evidenced by the refined anisotropic Lorentzian broadening along [010]. For $Bi_{0.15}$-O-LT, the refined values were LY = 14.7(3) and STEC = −2.0(3), but for $Bi_{0.15}$-M-LT, the refinement converged to LY = 25.4(2) and STEC = −12.2(2). There are few nonoverlapping peaks for $Bi_{0.15}$-M-LT, and some are quite broad. For instance, the $(20\bar{2})$ peak at 1.90 Å has fwhm of 0.039°, Figure 3b. However, many other peaks for that phase, such as (040) also shown in Figure 3b, are much sharper. The Stephens's formalism[25] inside GSAS was again used to deal with the anisotropic broadening.

There is a strong overlap between peaks of $Bi_{0.15}$-O-LT and $Bi_{0.15}$-M-LT as the unit cells are very similar. However, due to the ultrahigh-resolution SXRPD a refinement of the two similar phases was easily carried out. Initially, the positional and isotropic thermal parameters were refined by keeping the stoichiometry of both phases fixed to the values obtained for $Bi_{0.15}$-O-HT. To check the cation stoichiometry of both phases, the cation distribution of Bi and Ca was finally allowed to vary freely. This refinement improved the fit of both patterns considerably.

Table 4. Refined Structural Parameters for $Bi_{0.15}$-O-LT

atom	occ fac	x	y	z	U_{iso}
Bi	0.125(6)	0.0378(2)	1/4	−0.0060(4)	0.0055(3)
Ca	0.897(27)	0.0378	1/4	−0.0060	0.0055
Mn	1.0	0	0	1/2	0.0020(1)
O(1)	1.0	0.4832(6)	1/4	0.0713(8)	0.0029(9)
O(2)	1.0	0.2890(5)	0.3476(4)	0.7069(6)	0.0042(7)

Table 5. Refined Structural Parameters for $Bi_{0.15}$-M-LT

atom	occ fac	x	y	z	U_{iso}
Bi(1)	0.186(8)	−0.0349(3)	1/4	0.0040(3)	0.0013(7)
Ca(1)	0.671(35)	−0.0349	1/4	0.0040	0.0013
Bi(2)	0.180(8)	0.5362(3)	1/4	0.5090(3)	−0.0006(7)
Ca(2)	0.692(34)	0.5362	1/4	0. 5090	−0.0006
Mn(1)	1.0	1/2	0	0	−0.0025(6)
Mn(2)	1.0	0	0	1/2	0.0014(6)
O(11)	1.0	0.0156(7)	1/4	0.5630(8)	0.0011(9)
O(12)	1.0	0.4898(7)	3/4	0.0673(8)	−0.0038(8)
O(21)	1.0	0.7154(5)	0.0371(4)	0.2863(6)	0.0036(7)
O(22)	1.0	0.7888(5)	0.5342(4)	0.7876(6)	0.0007(6)

Table 6. Selected Bond Distances (Å) and Angles (deg) for $Bi_{0.15}$-O-LT

A−O(1)	2.404(4)	A−O(2) × 2	2.580(4)	Mn−O(1) × 2	1.9102(9)
A−O(1)	2.315(5)	A−O(2) × 2	2.585(4)	Mn−O(2) × 2	1.905(3)
A−O(1)	2.979(3)	A−O(2) × 2	2.339(3)	Mn−O(2) × 2	1.930(3)
		Mn−O(1)−Mn	156.6(3)	Mn−O(2)−Mn	155.7(2)

The final joint refinement was very good, R_{WP} = 4.16%, R_F^{O-LT} = 2.12%, and R_F^{M-LT} = 2.23% for the SXRPD data and R_{WP} = 5.48%, R_F^{O-LT} = 1.84%, and R_F^{M-LT} = 1.91% for the NPD data. The refined weight fractions were 67.7(6)% $Bi_{0.15}$-M-LT, 28.8(3)% $Bi_{0.15}$-O-LT, and 3.5(1)% $CaMn_2O_4$. In Figure 5 are shown the fits of the SXRPD (a) and NPD (b) patterns. The cell parameters and the peak shape coefficients are in Table 1. Refined atomic parameters are given in Tables 4 and 5 for $Bi_{0.15}$-O-LT and $Bi_{0.15}$-M-LT, respectively. Selected bond distances and angles are given in Tables 6 and 7.

Thermal Study. The evolution of the cell parameters at low temperature was determined from medium resolution *T*-variable NPD data (D20 diffractometer). The results from the Rietveld refinements are depicted in Figure 6. $Bi_{0.15}$-O-LT was taken into account, but the errors in this minor phase were large and the cell parameters are not reported here. The $Bi_{0.15}$-O-LT/$Bi_{0.15}$-M-LT phase ratio was kept fixed to the value obtained with SXRPD data. The β angle for $Bi_{0.15}$-M-LT is not shown as it displays a small temperature variation. To evaluate the accuracy of the obtained cell parameters, the lattice constants obtained in the joint SXRPD and NPD refinements are also given in Figure 6.

Discussion

Our experience with these and others high-resolution SXRPD data indicates that the anisotropic broadening is much better taken into account using Stephens's formalism.[25] The improvement of the fits, by using a better description of the peak shape, is much pronounced when sample-dependent effects are highlighted. For example, the isotropic Rietveld refinement of the "$Bi_{0.15}Ca_{0.85}MnO_3$" SXRPD data at 300 K converged to R_{WP} = 4.42%, the anisotropic refinement with ellipsoidal correction along [010] to R_{WP} = 3.96%, and the anisotropic refinement with the Stephens's formalism to R_{WP} = 3.52%. This improvement, ΔR_{WP} = 0.44%,

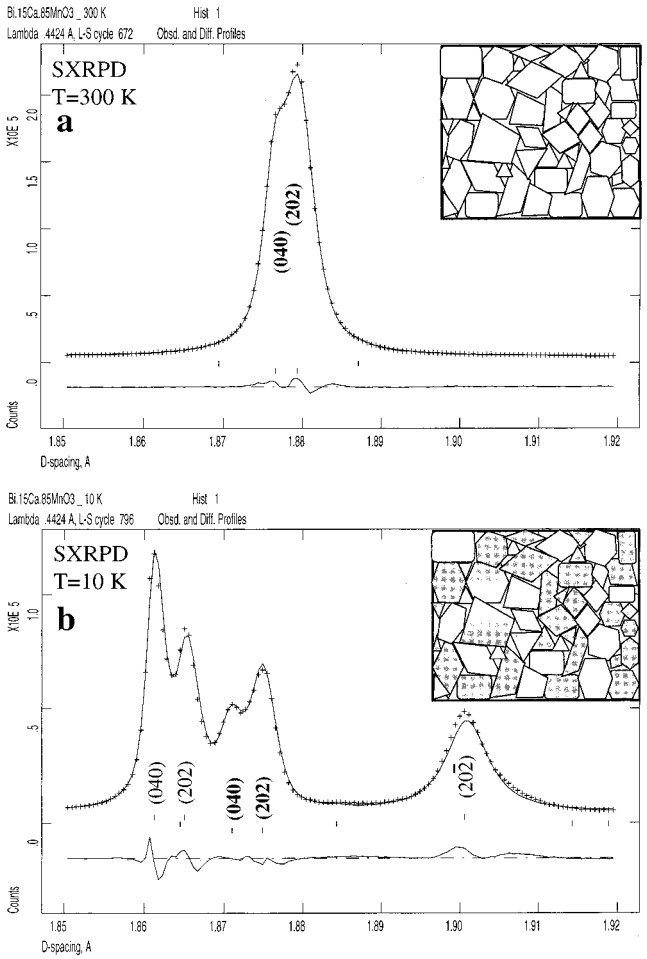

Figure 3. Selected region (1.85−1.92 Å) of the SXRPD Rietveld plot for "$Bi_{0.15}Ca_{0.85}MnO_3$" at (a) 300 K and (b) 10 K. The inset shows schematically the particle distribution with all domains being orthorhombic at 300 K and some being monoclinic (dark gray) and others remaining orthorhombic (pale gray) at 10 K.

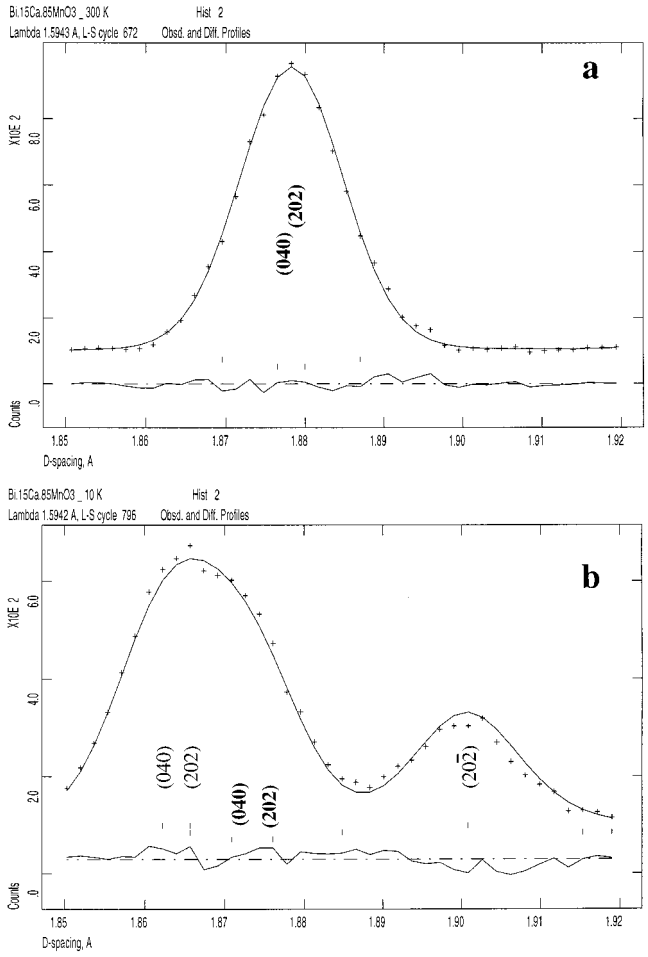

Figure 4. Selected region (1.85−1.92 Å) of the NPD Rietveld plot for "$Bi_{0.15}Ca_{0.85}MnO_3$" at (a) 300 K and (b) 10 K.

is noteworthy. However, for the refinement of the "$Bi_{0.15}Ca_{0.85}MnO_3$" SXRPD data at 10 K, the numbers are 7.47, 6.40, and 4.16%, respectively. Here, the improvement, $\Delta R_{WP} = 2.24\%$, is outstanding. The best possible refinement is essential to discuss subtle phenomena such as cation or anion vacancies, orbital ordering effects, magnetostriction, etc.

The joint refinement of $Bi_{0.15}$-O−HT with the nominal composition converged to $R_{WP}{}^{SXRPD} = 3.64\%$ and $R_{WP}{}^{NPD} = 5.17\%$. The *R*-factors for the refinement with free Bi and Ca contents were given above. So, the improvement [$\Delta R_{WP}{}^{SXRPD} = 0.12$ and $\Delta R_{WP}{}^{NPD} = 0.13\%$] is small but nonnegligible. Furthermore, it was shown in Figure 2 that this model gave the right intensity to some low-intensity peaks. Hence, $Bi_{0.15}$-O−HT is nonstoichiometric with calcium vacancies at the A-site. The average value for these vacancies is ~8%. This is not surprising as many manganites have been reported as nonstoichiometric due to cation vacancies mainly in the A-site.[29]

As shown in Figure 3, the 10 K SXRPD pattern clearly shows phase coexistence. It is common to describe this phenomenon as "macroscopic" phase segregation as the coherent diffraction domains have quite large sizes evidenced by "sharp" diffraction peaks. Minimum sizes can be estimated from Scherrer's formula by taking fwhm ~ 0.02°. This number, neglecting the instrumental contribution to the broadening which is the case, yields a minimum size of 1100 Å. Larger particles are in the sample as the broadening is *d**-dependent. The variation of the broadening with the diffraction angle allows one to distinguish between particle size broadening, Lorentzian but *d**-independent (LX and PTEC in GSAS), and broadening from microstrains which may also be Lorentzian but *d**-dependent (LY and STEC in GSAS). The term "microstrain" is normally a black box that accounts for many defects, and here compositional fluctuations, or chemical gradient, is a key parameter. Regions with slightly different chemical compositions have slightly different cell parameters which results in a pattern with broad peaks and their fwhms being *d**-dependent.

Some additional details about the microstructure of the samples can be obtained from the Williamson−Hall plot,[30] which has recently been used in manganites.[13] This approach relates the measured peak widths corrected from the instrumental broadening [fwhm (radians)] to the mean coherent diffraction domains [*L* (Å)] and the distribution of *d* spacings [$\Delta d/d$] for a selected class of reflections through the equation fwhm $\cos(\theta) =$

(29) Maguire, E. T.; Coats, A. M.; Skakle, J. M. S.; West, A. R. *J. Mater. Chem.* **1999**, *9*, 1346. DeSouza, R. A.; Islam, M. S.; Ivres-Tiffee, E. *J. Mater. Chem.* **1999**, *9*, 1621 and references therein.

(30) Williamson, G. K.; Hall, W. H. *Acta Metall.* **1953**, *1*, 22.

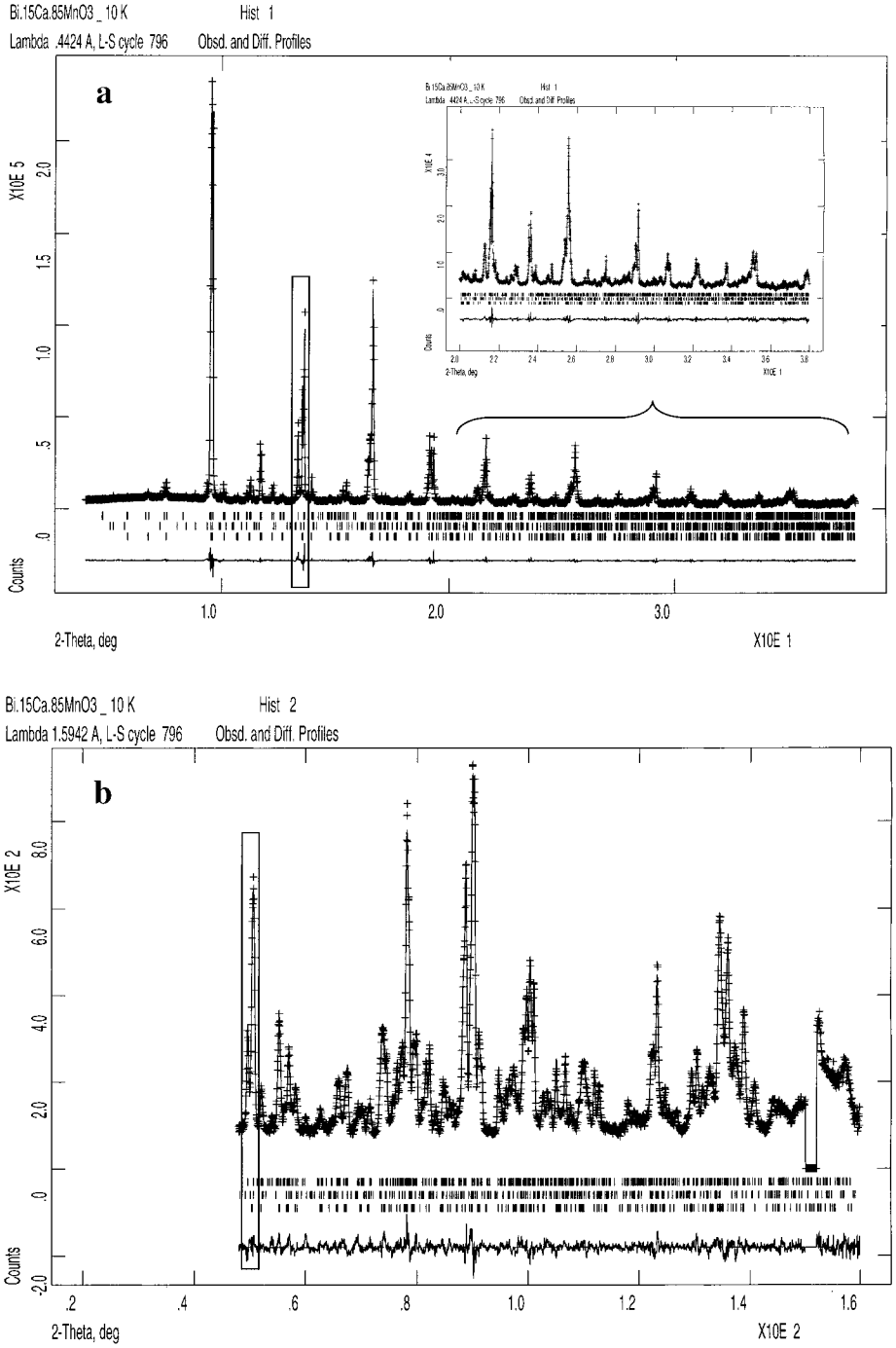

Figure 5. Observed (crosses), calculated, and difference SXRPD (a) and NPD (b) patterns for "$Bi_{0.15}Ca_{0.85}MnO_3$" at 10 K. Upper ticks are the allowed diffraction peaks for $Bi_{0.15}$-M-LT phase, intermediate ticks are those of the $CaMn_2O_4$ impurity phase, and lower ticks correspond to the $Bi_{0.15}$-O-LT phase. The inset shows the fit of the high-angle region (20−38°/2θ).

Table 7. Selected Bond Distances (Å) and Angles (deg) for $Bi_{0.15}$-M-LT

A(1)-O(11)	2.452(4)	A(1)−O(21) × 2	2.571(3)	Mn(1)−O(12) × 2	1.8959(8)
A(1)-O(12)	2.362(5)	A(1)−O(22) × 2	2.577(3)	Mn(1)−O(21) × 2	1.901(3)
A(1)-O(11)	2.975(5)	A(1)−O(22) × 2	2.341(2)	Mn(1)−O(22) × 2	1.945(3)
A(1)-O(12)	2.944(4)	A(2)−O(21) × 2	2.632(3)	Mn(2)−O(11) × 2	1.8922(8)
A(2)-O(11)	2.432(4)	A(2)−O(21) × 2	2.357(3)	Mn(2)−O(21) × 2	1.900(3)
A(2)-O(12)	2.353(4)	A(2)−O(22) × 2	2.552(4)	Mn(2)−O(22) × 2	1.932(3)
A(2)-O(11)	2.965(4)	Mn(2)−O(11)−Mn(2)	159.1(3)	Mn(1)−O(12)−Mn(1)	157.9(2)
A(2)-O(12)	2.979(4)	Mn(1)−O(21)−Mn(2)	156.6(2)	Mn(1)−O(22)−Mn(1)	157.3(1)

$(K\lambda/L) + 2(\Delta d/d)\sin(\theta)$, where K is a shape factor close to unity and λ is the wavelength of the experiment. We have carried out this study for two classes of reflections (220) and (022) in $Bi_{0.15}$-O-HT. By assumption of $K = 1$, the mean sizes of the coherent diffraction domains were 2500 and 2250 Å, respectively. From the slopes of the plots, $\Delta d/d$ were 9.6×10^{-4} and 8.3×10^{-4} for (220) and (022), respectively. For solid solutions, the $\Delta d/d$ term has a contribution from the chemical nature of the sample since a larger distribution of the unit cell values

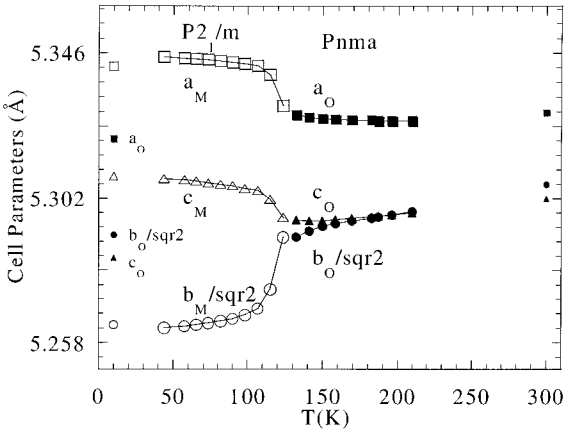

Figure 6. Temperature dependence of the unit cell parameters for "$Bi_{0.15}Ca_{0.85}MnO_3$" from the D20 NPD Rietveld refinements. The cells obtained at 300 and 10 K from the joint SXRPD and NPD studies are also shown. The cell evolution of $Bi_{0.15}$-O-LT is not shown.

due to chemical heterogeneity results in broader peaks. However, microstrains due to structural mistakes such as dislocations, stacking faults, microtwinings, and intergrowths are also included in this term which makes very difficult to quantify the chemical homogeneity from $\Delta d/d$ values. For comparison, the $\Delta d/d$ values of two samples of nominal stoichiometry $Nd_{1/2}Sr_{1/2}MnO_3$ are given.[13] One sample showed phase segregation on cooling ($\Delta d/d \sim 1.1 \times 10^{-3}$), and another sample, very carefully prepared, did not show phase segregation ($\Delta d/d \sim 5 \times 10^{-4}$). The $\Delta d/d$ values for $Bi_{0.15}$-O-HT are located between those numbers nearer to the chemical heterogeneous sample. Moreover, the same analysis has been carried out for a $Bi_{1/3}Ca_{2/3}MnO_3$ sample which shows OO and CO at low temperature, but it does not displays macroscopic phase segregation. The sample was prepared using the same procedure, and the synchrotron patterns were collected in the same experimental conditions. For $Bi_{1/3}Ca_{2/3}MnO_3$, a single SXRPD pattern is observed above and below T_{OO}. Again by assumption of $K = 1$, the mean sizes of the coherent diffraction domains were 3200 and 1800 Å, for (220) and (022), respectively. $\Delta d/d$ values were 1.1×10^{-3} and 6.8×10^{-4} for (220) and (022), respectively. These data shows that the chemical homogeneity of $Bi_{1/3}Ca_{2/3}MnO_3$ is similar to that of $Bi_{0.15}Ca_{0.85}MnO_3$.

The experiment was started with a single pattern/phase of $Bi_{0.15}$-O-HT as demonstrated in the result section. So, what mechanism can explain the phase segregation on cooling? Atomic diffusion across ~2000 Å at 120 K is absolutely ruled out. So, only two possibilities can explain the observed two-phase behavior: (1) Both phases are present at RT, but they are masked and only one average phase is evident even with ultrahigh-resolution SXRPD. (2) A homogeneous phase is present at RT, and when the structural transition takes place, large strain develops between the nucleation centers ($Bi_{0.15}$-M-LT) and the pristine bulk material ($Bi_{0.15}$-O-T), which prohibits the complete sample volume to transform. A phenomenon closely related to the martensitic phase transitions where metastable unchanged small domains coexist with the stable transformed phase.

Our high-resolution data and the joint refinement indicate that the first explanation is the correct one. First, the Rietveld refinement converged to different cation stoichiometries for $Bi_{0.15}$-M-LT and $Bi_{0.15}$-O-LT. Although with nonnegligible errors due to the strong overlapping, $Bi_{0.15}$-O-LT is almost stoichiometric and the calcium vacancies are concentrated in $Bi_{0.15}$-M-LT; see Tables 4 and 5. In this context is noteworthy to mention that a calcium richer sample with nominal composition "$Bi_{0.125}Ca_{0.875}MnO_3$", also studied by high-resolution SXRPD, displayed at 10 K $Bi_{0.125}$-O-LT as the major phase (84.8%) with $Bi_{0.125}$-M-LT as the minor one (15.2%). Second and very important, if the strain between the domains would be the key parameter, then the microstrain terms of $Bi_{0.15}$-O−HT should be smaller than those of strained $Bi_{0.15}$-O-LT, which it is not the case; see Table 1. Conversely, *the peaks of $Bi_{0.15}$-O-LT are sharper than those of $Bi_{0.15}$-O−HT*. These results demonstrate that the origin of the strains, and consequently of the observed broadening, is mainly due to compositional fluctuations and not due to phase mismatch. This result is entirely consistent with two specific and independent observations found for $Bi_{0.15}$-M-LT. Its SXRPD pattern has broader peaks (line-shape study), and the structure is more nonstoichiometric (SXRPD and NPD peak intensities study).

Macroscopic phase segregation below T_{OO}, commonly found in many manganites, may be due to chemical heterogeneity of the samples which contain domains/particles with slightly different electronic concentrations. At RT, the powder pattern looks single phase because the orthorhombic $GdFeO_3$-like structure is the stable atomic arrangement and only a dispersion of the unit cell values is detected by the probing radiation which yields a unique pattern broadened by microstrains (if the data have enough resolution to show it). A single pattern gets then automatically associated to a single homogeneous phase. This is schematically shown in the inset of Figure 3a, where the particles with the same powder pattern have the same gray aspect. However, when the synthesized nominal stoichiometry is close to a boundary where different thermal behaviors take place, then phase segregation phenomena can show up. Domains, with slightly different stoichiometries, undergo different thermal evolutions. At the transition temperature, the phase segregation suddenly comes into sight. These phases/domains are already in the sample at all temperatures, but only a structural transition unmasks the domains. This is schematically shown in the inset of Figure 3b, where the particles depicted as dark gray stand for $Bi_{0.15}$-M-LT and remaining particles depicted as pale gray stand for $Bi_{0.15}$-O-LT. These phases can be distinguished at 10 K because of the phase transition undergone by the $Bi_{0.15}$-M-LT crystallites. Noteworthy, $Bi_{1/3}Ca_{2/3}MnO_3$ has a chemical heterogeneity similar to that of $Bi_{0.15}$-O-HT but as it is not located near to a boundary of thermal behavior, macroscopic phase segregation does not take place. To measure the chemical heterogeneity of such domains with sizes of 1000−2000 Å is a challenge for electron microscopy. Domains with approximately the same dimensions have been detected at low temperature by electron microscopy[6] and scanning tunneling spectroscopy,[7] but the compositional fluctuations could not be established.

This macroscopic phase segregation is indeed common in complex solid solution, but it is not necessarily universal. However, to identify this behavior is difficult. Low-temperature characterization is needed, and even, so, routine NPD data from D2B, Figure 4b, do not show the phase coexistence. Laboratory Cu $K\alpha_{1,2}$ radiation has usually not enough resolution to show up this effect. Low-temperature very high resolution studies, for instance NPD data using longer wavelengths or strictly monochromatic Cu $K\alpha_1$ X-rays or synchrotron radiation, are needed to detect this type of phase coexistence. Alternatively, other techniques such as microscopy can reveal the heterogeneity, but to assign that to the corresponding phases is not easy. Data coming from techniques probing local features, such as solid NMR, EXAFS, and others, should be interpreted very cautiously as, in principle, they cannot distinguish between the two types of phase segregation, nano- and macroscopic, discussed in the Introduction. So, misinterpretation of the results may be an important issue when characterizing inhomogeneous electronic states in samples thought to be chemically homogeneous because they have a unique powder pattern at RT.

The synthesis was carried out with good care to have a homogeneous material, but it was obviously not achieved. So, a new question can be raised: if a single well-shaped pattern at RT is not enough to guarantee a homogeneous material, when should we stop a synthetic procedure? We cannot answer such a question, but keeping the sample at very high temperature for extremely long times is not always the more appropriated approach because some components can be lost due to volatilization. "Chimie douce" approaches such as sol−gel methods are probably better synthetic routes to ensure compositional homogeneity. This should be tested with a very high resolution diffraction characterization at low temperature.

The driving force of the structural transitions which unmask the domains is the orbital ordering. It is well established that most mixed-valent manganites undergo orbital ordering on cooling. The e_g electrons, itinerant above the transition temperature, become localized at low temperature with the concomitant anisotropic bond reorganization in the oxygen environment of the manganeses. This cooperative atomic rearrangement can change the symmetry, or not, depending upon the particular electronic concentration and orbital occupancy of the domains and the cation average size and distribution in the A site.

It has also been reported[18] that the $Bi_{1-x}Ca_xMnO_3$ series shows phase coexistence at low temperatures in a large compositional range near to $x = 0.15$ in agreement with our results. The compositional fluctuations in this series are not only due to a variable Bi/Ca ratio (x) in different particles but also due to the existence of domains with A-site vacancies also inducing chemical heterogeneity. In compounds such as $Nd_{0.5}Sr_{0.5}MnO_3$,[13] the chemical fluctuations are mainly due to different Nd/Sr ratios in the particles. However, for heavily doped manganites, the A (and sometimes even B) site vacancies[29] are very important which allows one to justify the compositional range, based on x, where phase coexistence is found. It should be noticed that A-site vacancies alter the electronic concentration of the domains (mean manganeses valence) three times more than M^{III}/A^{II} compositional fluctuations. More synthetic studies on heavily doped manganites are necessary to clarify the presence of cation vacancies in the different preparation conditions and to further understand the role of the A-site vacancies in the structural, electronic, and magnetic properties.

The structural differences between $Bi_{0.15}$-O-HT and $Bi_{0.15}$-O-LT are very subtle but detectable. Upon cooling, the structure changes as it is evident in the MnO_6 octahedra. In $Bi_{0.15}$-O-HT, the MnO_6 octahedra are almost regular with six Mn−O bond lengths of ∼1.915 Å, Table 2. However, the MnO_6 octahedra are tretragonally elongated with four short bonds of ∼1.908 Å and two longer bonds of ∼1.930 Å, Table 6, in $Bi_{0.15}$-O-LT. This is the manifestation of the static Jahn−Teller effect. The unit cell parameters slightly contract on cooling as shown in Figure 6.

The structural changes between $Bi_{0.15}$-O-HT and $Bi_{0.15}$-M-LT are much larger. Upon orbital ordering, the key parameter to follow is the b-axis which decreases strongly, as expected. The a and c axes slightly expand across the transition, Figure 6 and Table 1. As for $Bi_{0.15}$-O-LT, the structural changes are also evident in the MnO_6 octahedra. In orbital-ordered $Bi_{0.15}$-M-LT, the two crystallographically independent MnO_6 octahedra are tretragonally elongated with four short bonds of ∼1.90 Å and two long bonds of ∼1.93 Å, Table 7. This is again the manifestation of the static Jahn−Teller effect. Although two manganese sites are present in $Bi_{0.15}$-M-LT, the environments are very similar. Furthermore, we have not detected superstructure peaks due to the periodic long range order of Mn^{3+} and Mn^{4+}. Hence, $Bi_{0.15}$-M-LT displays orbital ordering but it does not show the typical signatures of charge-ordering.

Concomitantly with the orbital ordering, both $Bi_{0.15}$-O-LT and $Bi_{0.15}$-M-LT become antiferromagnetically ordered. LT-NPD data allowed one to determine the spin arrangements in the two phases that were different. The $Bi_{0.15}$-O-LT and $Bi_{0.15}$-M-LT phases show a G-type and C-type magnetic structures, respectively. The FULLPROF program was used to fit the magnetic diffraction peaks by Rietveld refinement. $Bi_{0.15}$-O-LT displays a G-type magnetic structure[31] characterized by an AFM coupling between neighboring Mn ions along the three directions of the pseudocubic axis. This is the spin ordering of orthorhombic $CaMnO_3$ with $T_N = 122$ K and 100% Mn^{4+}.[31,32] However, the ordered moment found in $Bi_{0.15}$-O-LT ($m_x = 1.24\ \mu_B$/Mn) is far from its theoretical saturation value, 3.2 μ_B. Mn spins in $Bi_{0.15}$-M-LT also order below $T_N \sim 125$ K. The magnetic structure is C-type with antiferromagnetic planes ferromagnetically coupled. Related to the monoclinic symmetry, the AFM planes are parallel to $(10\bar{1})$. This can be compared to the C-type ordering of $Pr_{0.25}Ca_{0.75}MnO_3$[33,34] or $Nd_{0.25}Sr_{0.75}MnO_3$[35] where the AFM planes are parallel to (010). As a consequence, the magnetic

(31) Wollan, E. O.; Koehler, W. C. *Phys. Rev.* **1955**, *100*, 545.
(32) Jirák, Z.; Krupicka, S.; Simsa, Z.; Dlouha, M.; Vratislav, S. *J. Magn. Magn. Mater.* **1985**, *53*, 153.
(33) Martin, C.; Maignan, A.; Damay, F.; Hervieu, M.; Raveau, B. *J. Solid State Chem.* **1997**, *134*, 134.
(34) Maignan, A.; Martin, C.; Damay, F.; Raveau, B. *Chem. Mater.* **1998**, *10*, 950.
(35) Kajimoto, R.; Yoshizawa, H.; Kawano, H.; Kuwahara, H.; Tokura, Y.; Ohoyama, K.; Ohashi, M. *Phys. Rev. B* **1999**, *60*, 9506.

cell of $Bi_{0.15}$-M-LT has the *a* and *c* axes doubled with respect to the nuclear cell. At 5 K the ordered moment is 2.7 μ_B/Mn ion, perpendicular to the AFM $(10\bar{1})$ planes. A detailed discussion of the magnetic and electrical properties for the highly doped $Bi_{1-x}Ca_xMnO_3$ series will be reported elsewhere.

Conclusions

Phase coexistence exists in "$Bi_{0.15}Ca_{0.85}MnO_3$" at all temperatures, but it is only detected, by diffraction, after the phase transition due to the orbital ordering. "$Bi_{0.15}Ca_{0.85}MnO_3$" contains particle sizes of ~2000 Å and slightly different calcium contents. The different electronic concentration in the particles explains the different thermal evolution on cooling which unmasks the domains. This work has established that a single-phase diffraction pattern at RT does not ensure chemical homogeneity in manganites. Hence, chemists lose the criterion to know when to stop a synthetic procedure. Furthermore, many studies dealing with macroscopic/nanoscopic phase separation have to be revisited. Materials were assessed to be homogeneous because they displayed a single powder diffraction pattern at RT. We have showed that this not necessarily the case and low-temperature very high-resolution diffraction experiments are necessary to rule out chemical inhomogeneity.

Acknowledgment. Financial support by the CICyT (Grants MAT97-0699 and MAT97-326-C4-4), MEC (Grant PB97-1175), and Generalitat de Catalunya (Grant GRQ95-8029) projects is acknowledged. ESRF and ILL are thanked for the provision of X-ray synchrotron and neutron powder diffraction facilities, respectively.

CM000440P